



Open camera or QR reader and scan code to access this article and other resources online.

ORIGINAL ARTICLE

Magnetic Soft Helical Manipulators with Local Dipole Interactions for Flexibility and Forces

Michiel Richter,¹ Mert Kaya,^{1,2} Jakub Sikorski,¹ Leon Abelmann,^{3,4} Venkatasubramanian Kalpathy Venkiteswaran,¹ and Sarthak Misra^{1,2}

Abstract

Magnetic continuum manipulators (MCMs) are a class of continuum robots that can be actuated without direct contact by an external magnetic field. MCMs operating in confined workspaces, such as those targeting medical applications, require flexible magnetic structures that contain combinations of magnetic components and polymers to navigate long and tortuous paths. In cylindrical MCM designs, a significant trade-off exists between magnetic moment and bending flexibility as the ratio between length and diameter decreases. In this study, we propose a new MCM design framework that enables increasing diameter without compromising on flexibility and magnetic moment. Magnetic soft composite helices constitute bending regions of the MCM and are separated by permanent ring magnets. Local dipole interactions between the permanent magnets can reduce bending stiffness, depending on their size and spacing. For the particular segment geometry presented herein, the local dipole interactions result in a 31% increase in angular deflection of composite helices inside an external magnetic field, compared to helices without local interactions. In addition, we demonstrate fabrication, maneuverability, and example applications of a multisegment MCM in a phantom of the abdominal aorta, such as passing contrast dye and guidewires.

Keywords: magnetic continuum manipulators, local dipole interactions, Cosserat rods, magnetic moment, flexibility

Introduction

CONTINUUM MANIPULATORS (CMs) rely on deformation of their elastic structure for motion and task execution.¹ CMs have found applications in medicine with varying methods of actuation, such as mechanical, fluidic, and magnetic.^{2,3} For example, precurved concentric tubes have been proposed for

transnasal surgery,⁴ tendon-driven catheters for cardiac steering,^{5,6} and hydraulically- and pneumatically-actuated CMs for endoscopy.^{7,8} A drawback of aforementioned CMs is the need for on-board actuators such as cables and fluidic circuitry. More recently magnetic actuation has been explored for contactless actuation of magnetic CMs (MCMs) during cardiovascular navigation,^{9–13} cardiac ablation,^{14,15} subretinal

¹Surgical Robotics Laboratory, Department of Biomechanical Engineering, University of Twente, Enschede, The Netherlands.

²Surgical Robotics Laboratory, Department of Biomedical Engineering, University of Groningen, and University Medical Centre Groningen, The Netherlands.

³KIST Europe Forschungsgesellschaft mbH, Saarbrücken, Germany.

⁴MESA+ Research Institute, University of Twente, Enschede, The Netherlands.

injections,¹⁶ atherectomy,¹⁷ capsule drug delivery,¹⁸ shaping variable stiffness guiding sheaths,¹⁹ and endoscopy.^{20–22}

MCM actuation relies on interaction with an external magnetic field,²³ and is suitable for traversing tortuous paths.²⁴ However, the field required for actuation is important to consider for medical applications. The space inside an operating room constrains the size of a magnetic actuation system,^{14,25} and the required field depends on MCM design and application.

Previous designs of MCMs use rigid permanent magnet(s)^{15,24,26,27} or magnetic polymer composite (MPC),^{9,28} integrated at the tip of CMs. MPC consists of magnetic microparticles suspended in an elastomer base. The volume fraction of magnetic particles, as well as their magnetization profile, can be predefined to achieve preprogrammed behavior of MPC robots.^{29–31} As such, a wide range of motion may be achieved in an external magnetic field.^{32–34} Although the material used in MCMs can vary, most designs have a slender cylindrical geometry and use either rigid magnets or MPC. For slender designs, that is, where the MCM length is significantly bigger than the diameter, magnetic volume and moment decreases. Reducing magnetic moment decreases the magnitude of exerted magnetic forces and torques. The gained flexibility inherent to a slender design compensates for the reduction in torque,^{9,16,24} but at the cost of reduction in actuation force.^{15,35}

Material properties that affect magnetic moment are (average) magnetization and volume. For cylindrical MCMs, magnetic moment and bending stiffness scale with the second and fourth power of radius, respectively. Magnetization scales linearly with magnetic volume fraction, but at an exponential cost in bending stiffness.⁹ Therefore, bending stiffness increases at higher rate than magnetic moment with diameter. Stiffness can be partially compensated by interaction between internal magnets, that is, local dipole interactions, which cause forces and torques exerted between segments of the MCM to affect its elasticity.³⁶ To the authors' best knowledge, using dipole interactions in MCMs to directly reduce bending stiffness, as well as indirectly increasing magnetic moment, has not yet been explored.

We present an MCM design to enable increasing diameter without compromising on bending flexibility, magnetic moment, and thereby magnetic pulling forces. The proposed design combines MPC single helices with intermittent permanent ring magnets, assembled over a flexible tube (Fig. 1). We investigate the local dipole interaction effect on promoting or opposing deflection of segments. We fabricate an MCM with the proposed design and quantify exerted magnetic forces by an external permanent magnet. Finally, we demonstrate maneuverability of the MCM inside a phantom of the abdominal aorta and use the central channel of the tube to show example applications, such as contrast dye injection and guidewire delivery.

Herein the MCM segment design is presented, followed by a general outline on Cosserat rod modeling of segments (Theory section). We implement the model, choose geometrical properties of MPC helices based on simulations and workspace constraints, and present fabrication of segments and a multisegment MCM (Methods section). This is followed by measuring the dipole interaction effect on the deflection response of segments in an external magnetic field. Maneuverability and example applications of the MCM design are demonstrated in a silicone phantom of the abdominal

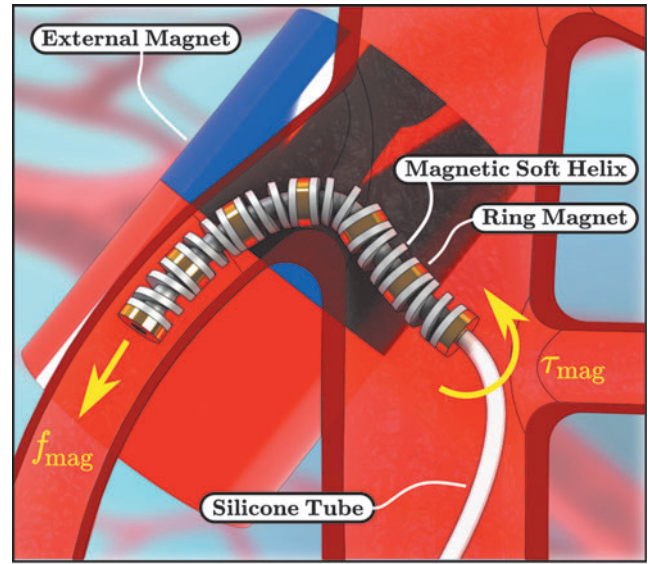


FIG. 1. Multisegmented MCM. The MCM consists of a series of segments containing ring magnets and magnetic soft helices. Segments are assembled on a hollow backbone that provides an open central channel. The magnetic moment of the structure allows propagation by a magnetic force (f_{mag}). In addition, the helical design provides an inherent flexibility that readily deflects in response to magnetic torque (τ_{mag}). The magnetic field for actuation is generated by an external magnet. MCM, magnetic continuum manipulator.

aorta (Results section). The presented theory and experiments provide design principles for devices based on assemblies of MPC and permanent magnets.

Theory

We present theory on segment design. In addition, a Cosserat rod model is discussed to simulate deflection response of segments in external fields.

Segment design

A segment comprises two ring magnets and an MPC helix shaped as a cored closed and ground compression spring (Fig. 2A). Ring magnets have predetermined length (L_{mag}). The helix contains a suspension of praseodymium-iron-boron (PrFeB) microparticles and polydimethylsiloxane (PDMS), has a length (L), radius (R), cylinder outer radius (r_{oc}), cylinder inner radius (r_{ic}), and number of windings (W). A helix boundary deflection angle (Θ) is assigned (Fig. 2B), giving a maximum deflection angle ($\theta = \Theta/W$) for each winding (Fig. 2D).

Dependent design variables of the helix are winding width ($w = R - r_{\text{oc}}$), height (h), and pitch ($p = R\theta$). The height necessary to achieve a desired L can be derived from the helix outer upper boundary curve,

$$\mathbf{u}(\beta) = \begin{bmatrix} x_u(\beta) \\ y_u(\beta) \\ z_u(\beta) \end{bmatrix} = \begin{bmatrix} R \cos(\beta) \\ R \sin(\beta) \\ \frac{\beta}{2\pi}(h+p) + h \end{bmatrix}, \quad (1)$$

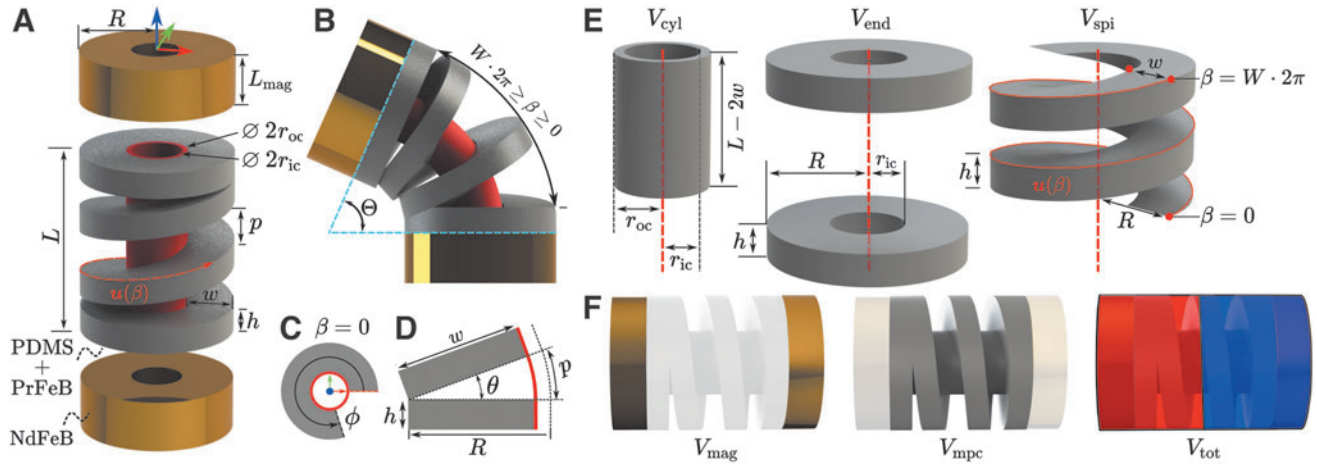


FIG. 2. Design of a magnetic segment. (A) Segments are made from MPC and NdFeB ring magnets. MPC contains a suspension of PDMS and PrFeB microparticles. The MPC is shaped as a closed and ground compression spring with a core cylinder. The spring/helix has an outer upper boundary curve ($u(\beta)$) and has windings ($W \in \mathbb{Z}^+$) with a width (w), height (h), and pitch (p). The core cylinder has an outer radius (r_{oc}), inner radius (r_{ic}), and a length (L). (B) Segment bending is limited to a boundary deflection angle (Θ). The helical part of the spring is described by revolution angle (β). (C) Transverse cross-section of the helix. MPC surrounds the core cylinder with a sector angle (ϕ). (D) Single pitch bending. With each pitch the helix can bend with $\theta = \Theta/W$ before adjacent windings touch. (E) Subvolumes of the MPC helix: the core cylinder (V_{cyl}), end disks (V_{end}), and spiral (V_{spi}). Subvolumes are used to compute total MPC volume. (F) Subvolumes of a segment: ring magnets (V_{mag}) and MPC helix (V_{mpc}). Combined volume is compared to total occupied volume (V_{tot}). Total occupied volume represents that of a reference solid cylindrical magnet with equal dimensions. MPC, magnetic polymer composite; NdFeB, neodymium-iron-boron; PDMS, polydimethylsiloxane; PrFeB, praseodymium-iron-boron.

where $\beta \in [0, 2\pi W + \phi]$ denotes the revolution angle with $\phi \in [0, 2\pi)$. The value of ϕ is chosen to achieve axially symmetric bending flexibility of the helix. We choose ϕ such that $w = z_u(\phi) - h$, because the ground ends have height (h). Rearranging to solve for ϕ gives

$$\phi = \frac{h}{h+p} 2\pi. \quad (2)$$

Since $z_u(\beta_{max}) = L$ ($\beta_{max} = 2\pi W + \phi$) we can derive from Equation (1) that

$$h = \frac{L - Wp}{2 + W}. \quad (3)$$

Given a segment design, we define a relative magnetic moment ($\mu_{rel} \in [0, 1]$) of an MCM as the ratio between magnetic moment of the MCM and a reference solid cylindrical magnet of equal length, diameter, and remanence of materials. The value μ_{rel} is dimensionless and describes the achievable magnetic moment of a segment/MCM design and is calculated from the relative absolute (V_{rel}) and magnetic (M_{rel}) volume:

$$V_{rel} = \frac{(S+1)V_{mag} + SV_{mpc}}{V_{tot}(S)}, \quad (4)$$

$$M_{rel} = \frac{(S+1)V_{mag} + S\Phi V_{mpc}}{V_{tot}(S)}, \quad (5)$$

$$\mu_{rel} = M_{rel} V_{rel}, \quad (6)$$

where $S \in \mathbb{Z}^+$ is the number of segments in an MCM, $V_{mag} = \pi(R^2 - r_{ic}^2)L_{mag}$ denotes ring magnet volume, V_{mpc} the MPC helix volume, $\Phi \in [0, 1]$ the volume fraction of PrFeB microparticles, and $V_{tot}(S) = \pi R^2(SL + (S+1)L_{mag})$ the reference magnet volume (Fig. 2F). The MPC helix volume (V_{mpc}) is computed from three smaller volumes (Fig. 2E): core cylinder (V_{cyl}), closed and ground ends (V_{end}), and spiral (V_{spi}),

$$V_{mpc} = V_{cyl} + V_{end} + V_{spi}, \quad (7)$$

as follows:

$$\begin{aligned} V_{cyl} &= \pi(r_{oc}^2 - r_{ic}^2)(L - 2h) \\ V_{end} &= 2\pi(R^2 - r_{ic}^2)h, \\ V_{spi} &= 2\frac{wh}{\phi} \int_0^\phi \beta \sqrt{R^2 + \dot{z}_u^2} d\beta + \\ &\quad wh \int_\phi^{2\pi W - \phi} \sqrt{R^2 + \dot{z}_u^2} d\beta, \end{aligned} \quad (8)$$

where $\dot{z}_u = \partial z_u / \partial \beta$.

Cosserat rod model

A Cosserat rod model is a continuum mechanics model used to compute statics and dynamics of CMs, comprehensively reported in the works by Till et al³⁷ and Edelmann et al.³⁸ Magnetic segments are characterized by a centerline parameter ($s \in [0, L + 2L_{mag}]$) and discretized into N sub-segments (Fig. 3A) of length (Δs_n) to obtain $N + 1$ centerline points (s_0, s_1, \dots, s_N). Each centerline point has associated material states: position ($\mathbf{p}_n \in \mathbb{R}^3$), orientation quaternion ($\mathbf{q}_n = (q_r, \mathbf{q}_i) \in \mathbb{H}$, $q_r \in \mathbb{R}$, $\mathbf{q}_i \in \mathbb{R}^3$), internal force ($\mathbf{n}_n \in \mathbb{R}^3$), and internal moment ($\mathbf{m}_n \in \mathbb{R}^3$). The evolution

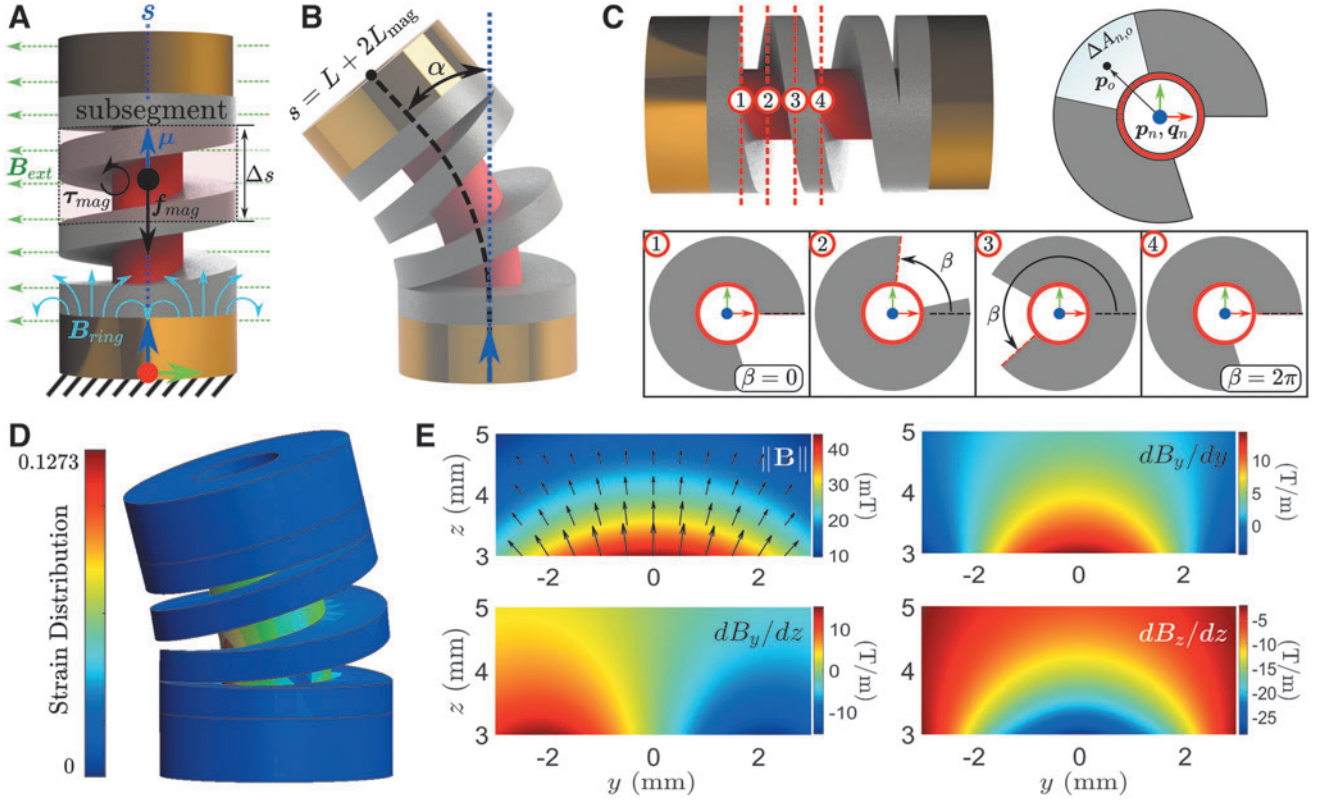


FIG. 3. Modeling of magnetic segments with Cosserat rods. **(A)** A segment with centerline parameter ($s \in [0, L + 2L_{\text{ring}}]$) is discretized into subsegments of length (Δs_n), with $n \in [0, 1, \dots, N]$. Each subsegment has a dipole moment (μ) and experiences a magnetic torque (τ_{mag}) and force (f_{mag}). The magnetic torques and forces are due to a homogeneous external magnetic field (B_{ext}) and nonhomogeneous magnetic field from the base ring magnet (B_{ring}). Both base and tip ring magnets have the same geometry and magnetic moment. **(B)** The segment responds to the magnetic field with tip deflection (α). **(C)** Cross sections (1–4) along the centerline show a rotating pattern as a function of the revolution angle (β). To compute magnetic forces and torque acting on the n th subsegment, the cross-sectional area is divided in discrete parts ($\Delta A_{n,o}$), $o \in [0, 1, \dots, O]$, with a center position (p_o) defined relative to the subsegment centerline pose (p_n, q_n). **(D)** Strain distribution of segments during deflection. **(E)** FEM estimates of the magnetic field (B_{ring}) in the yz -plane generated by the proximal ring magnet with outer diameter 4 mm, inner diameter 1.5 mm, and length 1 mm. The field magnitude and nonzero gradients are shown between 3 and 5 mm. Field directions are represented by the arrows. The fields and gradients are responsible for local dipole interactions with the segment tip ring magnet. FEM, finite element model.

of material states from s_{n-1} to s_n depends on a set ordinary partial differential equations.³⁸ Change in pose between subsegments is determined by shear/extension and bending/torsion stiffness matrices ($K_{\text{se}}, K_{\text{bt}} \in \mathbb{R}^{3 \times 3}$), as well as distributed external magnetic forces and torques ($f_{\text{mag}}, \tau_{\text{mag}} \in \mathbb{R}^3$), also called magnetic wrench.

Herein we extend existing static Cosserat rod models to account for nonhomogeneity of magnetic fields and gradients across the cross-sectional area of subsegments (Fig. 3A). The magnetic field ($B(p) \in \mathbb{R}^3$) is composed of a homogeneous external field ($B_{\text{ext}} \in \mathbb{R}^3$) and nonhomogeneous ring magnet field ($B_{\text{ring}}(p) \in \mathbb{R}^3$),

$$B(p) = B_{\text{ext}} + B_{\text{ring}}(p). \quad (9)$$

The total magnetic wrench on a subsegment is computed as the sum of distributed wrenches. Given a subsegment with pose (p_n, q_n), we discretize its cross-sectional area into smaller sector areas ($\Delta A_{n,o}$) with volumes ($\Delta V_{n,o} = \Delta A_{n,o} \Delta s_n \in \{\Delta V_{n,1}, \dots, \Delta V_{n,O}\}$). Each sector area has its own pose ($p_{n,o}, q_n$), where $p_{n,o} = p_n + R(q_n)p_o$, with

$R(q_n) \in SO(3)$ a rotation matrix associated with orientation quaternion (q_n) and p_o the xy -position in the center of $\Delta A_{n,o}$, respectively (Fig. 3C). Then the wrench is computed as

$$f_{\text{mag}}(p_n, q_n) = \sum_{o=1}^O \underbrace{\nabla \left(\frac{\partial \mu(q_n)}{\partial V} \cdot B(p_{n,o}) \right)}_{f_{\text{mag}}(p_{n,o}, q_n)} \Delta V_{n,o}, \quad (10)$$

$$\tau_{\text{mag}}(p_n, q_n) = \sum_{o=1}^O \left(\frac{\partial \mu(q_n)}{\partial V} \times B(p_{n,o}) \right) \Delta V_{n,o} + (p_{n,o} - p_n) \times f_{\text{mag}}(p_{n,o}, q_n),$$

with $\mu(q_n)$ the magnetic dipole moment of the subsegment with partial derivative

$$\frac{\partial \mu(q_n)}{\partial V} = \frac{\Phi B_r}{\mu_0} R(q_n) \hat{e}_3, \quad (11)$$

where μ_0 is the vacuum permeability, Φ the magnetic particle volume fraction, and B_r the magnetic particle residual flux

density. The sector-shaped cross-sections (Fig. 3C) exhibit a rotating pattern along s by a revolution angle (β). Defining $s_\beta \in [0, L - 2h]$ that starts on the level of $\beta = 0$ (Fig. 2E), the corresponding revolution angle can be found as $\beta = 2\pi W s_\beta / (L - 2h)$.

The magnetic wrench causes deflection (α) of magnetic segments (Fig. 3B). Magnitude of deformation is determined by shear/extension and bending/torsion stiffness matrices ($\mathbf{K}_{se}, \mathbf{K}_{bt}$) along the segment, defined as

$$\mathbf{K}_{se} = \begin{pmatrix} G_n & 0 & 0 \\ 0 & G_n & 0 \\ 0 & 0 & E_n \end{pmatrix} A_n, \quad \mathbf{K}_{bt} = \begin{pmatrix} E_n & E_n & 0 \\ E_n & E_n & 0 \\ 0 & 0 & G_n \end{pmatrix} \mathbf{J}_n, \quad (12)$$

where G_n and E_n are the material shear and elastic moduli, A_n is the cross-section area, and $\mathbf{J}_n \in \mathbb{R}^{3 \times 3}$ is a rotational inertia matrix.³⁷ The rotational inertia matrix is defined as

$$\mathbf{J}_n = \begin{pmatrix} I_{xx} & I_{xy} & 0 \\ I_{yx} & I_{yy} & 0 \\ 0 & 0 & I_{zz} \end{pmatrix}. \quad (13)$$

For MPC helices we consider only the end disks and the core cylinder, that is, we do not account for the spiral in computing the cross-sectional area or area moment of inertia for a cross-section, because the majority of strain during bending is concentrated in the core cylinder (Fig. 3D). For the core cylinder $I_{xx} = I_{yy} = \pi(r_{oc}^4 - r_{ic}^4)/4$, $I_{zz} = I_{xx} + I_{yy}$, and $I_{xy} = I_{yx} = 0$. For end disks and ring magnets $I_{xx} = I_{yy} = \pi(R^4 - r_{ic}^4)/4$, $I_{zz} = I_{xx} + I_{yy}$, and $I_{xy} = I_{yx} = 0$. Given the rotational inertia matrix, as well as the distributed magnetic wrench, the segment statics can be solved as a boundary value problem.³⁷

Methods

The Cosserat rod model is used to simulate deflection of magnetic segments by an external homogeneous magnetic field. Simulation results and design constraints are used to choose design parameters of segments. An MCM is assembled as a series of segments. Experiments are performed to validate the model, investigate the effect of local dipole interactions on segment flexibility, quantify forces on the MCM by an external permanent magnet, and demonstrate maneuverability of the MCM using magnetic wrenches exerted by the external permanent magnet.

Model-based segment design

In simulations, segments are considered fixed at the base and free at the tip (Fig. 3A). The previously described Cosserat rod model is implemented in MATLAB 2020B (MathWorks, Natick, MA, USA). Segments are simulated without a backbone. A perpendicular external uniform magnetic field ($\|\mathbf{B}_{ext}\| = 20$ mT) is applied together with a nonuniform local field (\mathbf{B}_{ring}) from the base ring magnet (Fig. 3A). Segment tip angular deflection (α) as a result of the magnetic wrench is computed (Fig. 3B). The ring magnet field is estimated from a finite element model in COMSOL 5.6 (COMSOL, Burlington, VT, USA), shown in Figure 3E. We estimate the magnetic field at positions (\mathbf{p}) in the yz -plane

above the ring magnet and fit a model to obtain an analytical description of the estimated field and gradients, representing the 3D field due to the axial symmetry of the ring magnet field.³⁹

Commercially available ring magnets are used (OD: 4 mm, ID: 1.5 mm), which constrains segment design accordingly. Material properties of ring magnets and MPC helices are listed in Table 1. The MPC consists of PDMS with predefined Shore A hardness ($H=33$) and magnetic volume fraction ($\Phi=0.25$). The PDMS elastic modulus and MPC shear modulus are determined by Gent's relation⁴⁰ and a Mooney-model,^{9,41} respectively,

$$E_{pdms} = \frac{0.0981(56 + 7.66H) \cdot 10^6}{0.137505(254 - 2.54H)}, \quad (14)$$

$$G_{mpc} = \frac{E_{pdms}}{2(1 + \nu)} \exp\left(\frac{2.5\Phi}{1 - 1.35\Phi}\right), \quad (15)$$

with constant Poisson ratio ($\nu = 0.40$).

Segment design variables are helix length (L) and boundary deflection angle (Θ), which determine relative magnetic moment (μ_{rel}) and deflection response (α) inside an external magnetic field. A range of lengths ($L_i \in L_1, \dots, L_l$) and boundary deflections ($\Theta_j \in \Theta_1, \dots, \Theta_j$) are considered. To demonstrate workspace-constrained segment design, we choose a phantom of the adult human abdominal aorta as the MCM navigation environment due to confinement, tortuosity, and path length (Fig. 4A). We impose that a multisegment MCM should be able to bend 120° within 15 mm for maneuverability and define a set of valid combinations as

$$\mathbb{S} = \{L_i, \Theta_j \mid \frac{120}{\Theta_j} L_i + \lfloor \frac{120}{\Theta_j} \rfloor L_{mag} \leq 15\}. \quad (16)$$

TABLE 1. SEGMENT DESIGN PARAMETERS AS USED IN THIS ARTICLE

| Quantity | Symbol | Value |
|-----------------------|-----------|------------|
| MPC helices | | |
| Helix length | L | 4 mm |
| Boundary deflection | Θ | 40° |
| Helix radius | R | 2 mm |
| Windings | W | 2 |
| Cylinder outer radius | r_{oc} | 0.95 mm |
| Cylinder inner radius | r_{ic} | 0.75 mm |
| PDMS shore hardness | H | 33 |
| PDMS Poisson's ratio | ν | 0.40 |
| Volume fraction | Φ | 0.25 |
| PrFeB remanence | B_r | 1 T |
| Ring magnets | | |
| Magnet length | L_{mag} | 1 mm |
| Magnet outer radius | R | 2 mm |
| Magnet inner radius | R | 0.75 mm |
| NdFeB remanence | B_r | 1.35 T |

Definitions are shown in Figure 2A. Remanence of NdFeB and PrFeB and material properties of PDMS are listed as used for simulations.

MPC, magnetic polymer composite; NdFeB, neodymium-iron-boron; PDMS, polydimethylsiloxane; PrFeB, praseodymium-iron-boron.

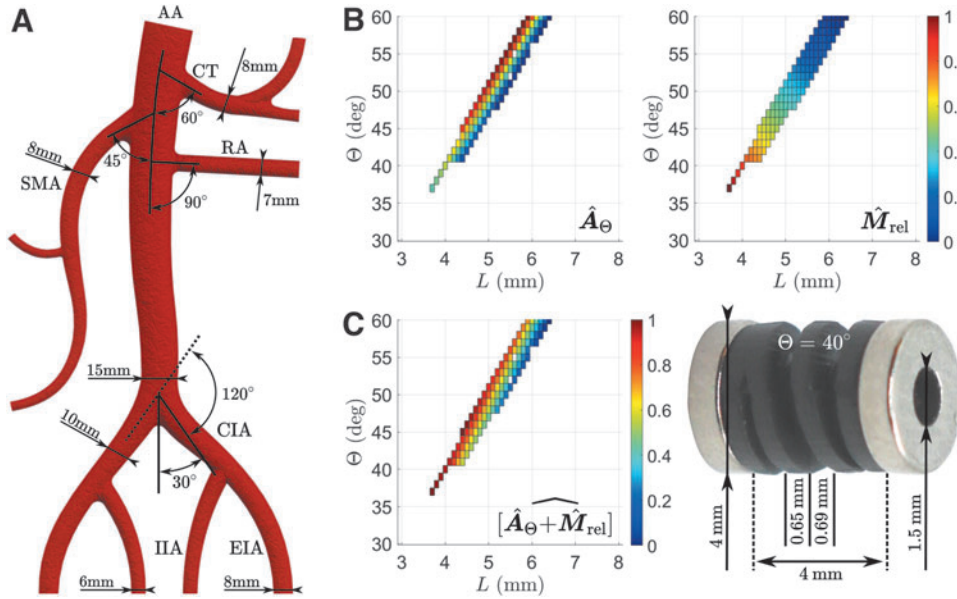


FIG. 4. Model-based design of magnetic segments. (A) A planar diagram of the AA with major branches: CT, SMA, RA. The aortic bifurcation gives rise to the CIA, leading to the IIA and EIA. Given vessel diameters and branching angles are within the ranges reported in literature. Design constraints are imposed on segments based on anatomical geometry. (B) Normalized simulation results of segment deflection ($\alpha(L_i, \Theta_j)$) and relative magnetic moment ($\mu_{\text{rel}}(L_i, \Theta_j)$), according to Equations (17) (\hat{A}_Θ) and (18) (\hat{M}_{rel}). Results are shown for combinations $L_i, \Theta_j \in \mathbb{S}$ [Equation (16)]. (C) Normalized sum of simulation results is chosen as a cost function to decide on helix length (L) and boundary deflection (Θ). A photograph of a final segment is shown with annotated dimensions. A complete list of dimensions and material properties is given in Table 1. AA, abdominal aorta; CIA, common iliac arteries; CT, celiac trunk; EIA, external iliac arteries; IIA, internal iliac arteries; RA, renal arteries; SMA, superior mesenteric artery.

Branching angles and vessel diameters of the phantom are within dimensions reported in literature.^{42–47} To match fabrication constraints, as well as ensure structural integrity of MPC helices, we set a minimum winding height ($h \geq 0.6$ mm) and height-to-pitch ratio ($h/p \geq 0.9$). Angular deflection ($\alpha(L_i, \Theta_j)$) is computed from segment tip orientation (\mathbf{q}_N) obtained from the BVP solution.³⁹ Relative magnetic moment $\mu_{\text{rel}}(L_i, \Theta_j)$ is computed with Equation (4).

From simulations we obtain matrices $\mathbf{A} \in \mathbb{R}^{I \times J}$ and $\mathbf{M}_{\text{rel}} \in \mathbb{R}^{I \times J}$ with components $\alpha(L_i, \Theta_j)$ and $\mu_{\text{rel}}(L_i, \Theta_j)$. Our aim is that $\alpha(L_i, \Theta_j) \rightarrow \Theta_j$ within the applied external field ($\|\mathbf{B}_{\text{ext}}\| = 20$ mT). We define an absolute deflection mismatch $A_{ij} = |\alpha(L_i, \Theta_j) - \Theta_j|$, giving $\hat{\mathbf{A}} \in \mathbb{R}^{I \times J}$ that is normalized to give highest weight to combinations $\{L_i, \Theta_j\}$ that provide $\alpha(L_i, \Theta_j) \rightarrow \Theta_j$,

$$\hat{A}_\Theta = \frac{|\tilde{\mathbf{A}} - \max(\tilde{\mathbf{A}})|}{\max(|\tilde{\mathbf{A}} - \max(\tilde{\mathbf{A}})|)}. \quad (17)$$

In addition, to increase the weight of high compared to low $\mu_{\text{rel}}(L_i, \Theta_j) \in \mathbf{M}_{\text{rel}}$, we normalize all values in \mathbf{M}_{rel} according to:

$$\hat{M}_{\text{rel}} = \frac{\mathbf{M}_{\text{rel}} - \min(\mathbf{M}_{\text{rel}})}{\max(\mathbf{M}_{\text{rel}}) - \min(\mathbf{M}_{\text{rel}})}. \quad (18)$$

Values in $\hat{\mathbf{A}}_\Theta$ and $\hat{\mathbf{M}}_{\text{rel}}$ for $L_i, \Theta_j \in \mathbb{S}$ are shown in Figure 4B. The combination $L = 4$ mm and $\Theta = 40^\circ$ is chosen based on a cost function ($\hat{\mathbf{A}}_\Theta + \hat{\mathbf{M}}_{\text{rel}}$). The relative magnetic moment of the MCM (μ_{rel}) for multiple segments ($S \in \mathbb{Z}^+$) is shown in

Figure 5, for designs with an open and closed core cylinder and helices without magnetic particles.

Fabrication

MPC consists of a base elastomer material with a suspension of ferromagnetic particles. We choose PDMS (Sylgard 184 silicone elastomer; Farnell, United Kingdom) of its low elastic modulus and biocompatibility.^{24,48} The secondary

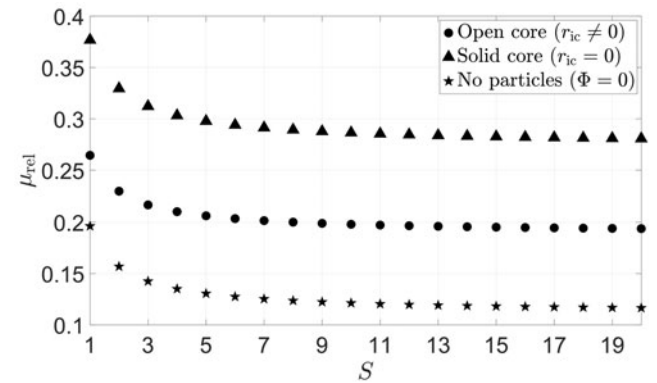


FIG. 5. Relative magnetic moment (μ_{rel}) of an MCM with $S \in \mathbb{Z}^+$ segments. The values of μ_{rel} are specific to CMs made from segments with design variables as listed in Table 1. Values are shown for three cases: segments with open ($r_{\text{ic}} = 0$) and closed ($r_{\text{ic}} \neq 0$) central core cylinders and segments without magnetic particles ($\Phi = 0$). The presented MCM ($S = 9$) has a relative magnetic moment of 0.2.

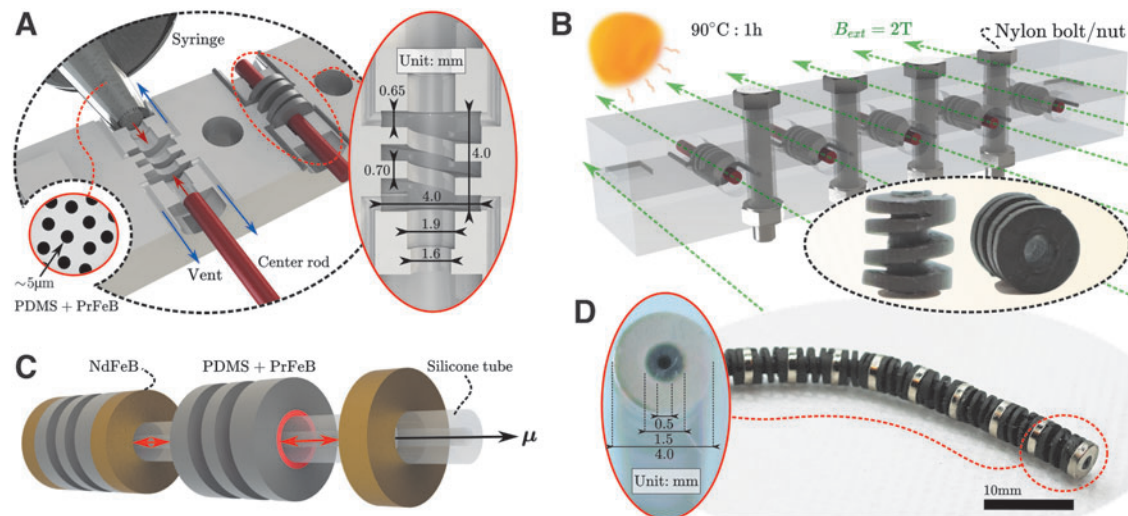


FIG. 6. Fabrication process of segments and the MCM. (A) Injection molding. A MPC mixture of PDMS and PrFeB microparticles is injected in a mold fabricated by means of stereolithography. The segment open central channel is obtained by placing a center rod to occupy the center of the mold. Thus, the MPC helix and core cylinder are part of the bulk helical structure and made of the same material. (B) The MPC inside the molds is heat cured and magnetized inside a 2T uniform external field. The center rods are subsequently pulled out to get the final MPC helices. (C) Assembly of the multisegment MCM. Permanent ring magnets and MPC helices are slid over a silicone tube and fixed in place with Loctite 401. (D) Final assembled multisegment MCM. Zoomed in frontal image of the MCM tip with 4 mm diameter, showing the silicone tube backbone (OD: 1.5 mm) with open central lumen (ID: 0.5 mm).

MPC ingredient is praseodymium microparticles (PrFeB) with an average diameter of 5 μm (MQFP-16-7-11277; Magnequench GmbH, Germany). PrFeB was chosen based on availability and can be interchanged with NdFeB for a higher remanent magnetization. The PDMS is mixed at base:curing agent ratio of 10:1, PrFeB added at a volumetric ratio (Φ) of 0.25, and the suspension degassed in a vacuum chamber.

A mold and center rods are printed (Form-2, Clear resin; Formlabs, USA) and baked at 120°C for 1 h to prevent PDMS curing inhibition.⁴⁹ The mold is treated with release spray (Ease Release 200; Smooth-On, Inc., USA) before MPC injection. The molding process is shown in Figure 6A and B. First, rods are placed in the molds, forcing injected MPC along the helical path. Second, rods are removed and the mold further filled with MPC. Third, rods are reintroduced and the MPC vulcanized at 90°C for 1 h. Finally, the molds are placed inside a uniform magnetic field of 2T, generated by an electromagnet (GMW 3474-140; GMW, Redwood City, CA, USA), to axially magnetize the MPC helices.

The multisegment MCM (Fig. 6C, D) is assembled by sliding MPC helices and N48 NdFeB ring magnets (ID: 1.5 mm, OD: 4 mm, $L_{\text{mag}} = 1$ mm [Neomagnete, Berlin, Germany]) over a silicone tube (ID: 0.5 mm, OD: 1.5 mm; Advanced Fluid Solutions, United Kingdom). The faces of ring magnets and helices are further adhered using Loctite 401.

Local dipole interactions and flexibility

To validate the Cosserat rod model and demonstrate the effect of local dipole interactions, we consider angular deflection of three different segments: helix, helix with a tip magnet, and helix with a base and tip magnet (Fig. 7A). The same helix is used to avoid variations between samples.

Segments are suspended horizontally in the workspace of an electromagnetic actuation system.⁵⁰

A perpendicularly oriented magnetic field is applied to deflect the segments. The workspace is recorded with two Dalsa Genie Nano RGB cameras (Teledyne Dalsa, Waterloo, Canada). Tip deflection is computed with a previously reported shape reconstruction algorithm.^{39,51} In addition, flexibility is demonstrated by comparing deflection of a three-segment MCM to that of an MPC cylinder. The MPC cylinder is made as a solid cylinder with $\Phi = 0.2$ to match the relative magnetic moment of the MCM (Fig. 5).

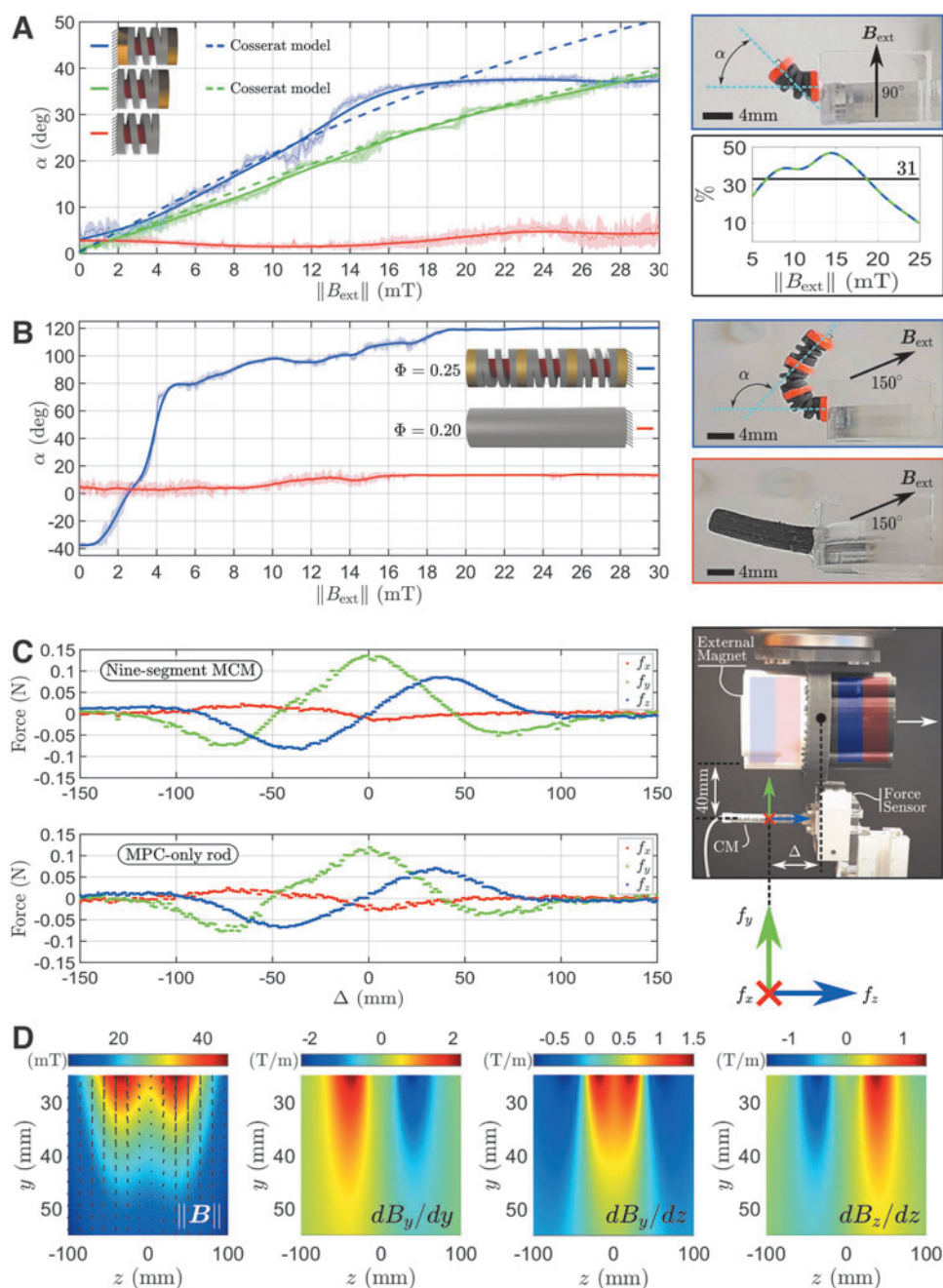
Magnetic forces on the multisegment MCM (Fig. 6D) are quantified using the setup shown in Figure 7C. The MCM is fixed in a rigid nonmagnetic holder and attached to a three-axis force sensor (K3D40; ME-Meßsysteme GmbH, Hennigsdorf, Germany). A cylindrical magnet (composed of two magnets: N45, 45 mm diameter, 30 mm length) is moved with a robotic arm in parallel over the MCM and an MPC-cylinder with equal length, diameter, and magnetic moment, from a distance of 40 mm.

To analyze the local dipole interactions between multiple ring magnets in an MCM, we simulate interaction between 2 and 5 ring magnets at various relative angles. Bending torques on the tip magnet due to the collective field and field gradients of preceding magnets are computed.

Phantom navigation

Maneuverability of the multisegment MCM is demonstrated inside a silicone vascular phantom using magnetic wrenches exerted by an external permanent magnet. The phantom is fabricated with silicone rubber (40 Shore A hardness; Siliconesandmore, The Netherlands) with a removable ABS scaffold.⁵² The phantom represents the

FIG. 7. Results showing local dipole interactions, flexibility, and exerted forces with external magnetic field and field gradients. **(A)** Angular deflection (α) of an MPC helix, MPC helix with tip magnet, and MPC helix with tip and base magnet. Mean measured (dotted, 12 measurements), standard deviation (shaded), best fit (solid), and model prediction (dashed) are shown. The best fit for the MPC helix with tip and base magnet shows a 31% increased tip deflection compared to the helix with only a tip magnet. **(B)** Angular deflection of a three-segment MCM and MPC cylinder with equal dimensions and relative magnetic moment. **(C)** Magnetic forces exerted on a nine-segment MCM and an MPC cylinder ($\Phi=0.2$) of similar dimensions and relative magnetic moment. An external magnet at a distance of 40 mm is moved in parallel over the MCM and rod. Measurements are shown for relative displacements (Δ). **(D)** External magnet field and nonzero field gradients in the zy -plane along the dipole axis (z) at distances (y) from the MCM.



abdominal aorta and its major branches. We lubricate the phantom with silicone oil to reduce friction. Pulsatile flow is mimicked with a peristaltic pump (ISM 404; Ismatec, Wertheim, Germany) and an emulsion of water and red food dye. Two example demonstrations are performed: flow-off and flow-on. With flow-off, delivery of a contrast dye simulant through the MCM backbone, as well as passing a guidewire in vessel bifurcations, is shown. For the demonstration with the guidewire (OD: 0.89 mm; Terumo Europe), the silicone tube backbone is replaced with a polytetrafluoroethylene backbone (ID: 1.4 mm, OD: 1.48 mm; Zeus, Inc.). During flow-on, the pulsatile flow of the pump is set to 2.7 L/min, which is within the physiological range found in the abdominal aorta.⁵³

Results

Experiments are performed to demonstrate the effect of local dipole interactions on bending flexibility of magnetic segments. Flexibility of the helical design is compared to an MPC cylinder with similar length, diameter, and magnetic moment. Forces on the MCM exerted by an external permanent magnet are quantified for demonstration of MCM maneuverability. Finally, maneuverability of the MCM is shown using magnetic wrenches exerted by an external magnet.

Local dipole interactions

Influence of local dipole interactions between ring magnets on the bending response of magnetic segments is demonstrated

by measuring tip angular deflection (α) for three different segments: MPC helix (red), helix and tip magnet (green), and helix with tip and base magnet (blue), shown in Figure 7A. Helices are designed to bend a maximum of $\Theta = 40^\circ$. For each field magnitude ($\|\mathbf{B}_{\text{ext}}\| \in [0, 30]$ mT) we reconstruct the segment tip deflection 12 times.³⁹ For the segment shown in Figure 7A, the addition of the base magnet reduces the required external field magnitude on average by 31% for similar deflection angle, in the range of 5–25 mT.

Cosserat model predictions of helix deflection with a tip and base magnet (dashed blue), and with only a tip magnet (dashed green), follow the measured deflections during the transient response (Fig. 7A). However, physical bending limitations imposed by Θ are not captured by the model. Therefore, the model may be inaccurate in modeling deflection response of multiple connected segments. Model and experimental results suggest that Cosserat rods can be used to predict the effect of local dipole interactions on the deflection response of single segments. Model versatility allows changing parameters such as magnetic particle concentration, helix and ring magnet dimensions, backbone, as well as magnetization direction, depending on the intended application. The model is available online at <https://github.com/MichielRichter/Magnetic-Soft-Helical-Manipulators>

Trade-off between magnetic moment and bending flexibility is demonstrated with deflection of a three-segment MCM and MPC cylinder of similar length, diameter, and magnetic moment (Fig. 7B). The three-segment MCM and MPC cylinder deflect on average 119° and 16° within 20 mT, respectively (Supplementary Video S1). The three-segment MCM has a relative magnetic moment (μ_{rel}) of 0.2, which is the same as the MPC rod ($\Phi = 0.2$). We note that a volume fraction of 0.2 for MPC rods has been reported optimal for bending.⁹ We observe an unequal amount of bending by segments as each preceding segment experiences additional torques from subsequent segments. This can be addressed by providing different magnetic volume fractions (Φ) to the helices.³⁴

Magnetic forces on the multisegment MCM (Fig. 6D) are quantified and compared to an MPC cylinder (0.2 volume fraction) of similar length, diameter, and magnetic moment, using the setup shown in Figure 7C. Forces are exerted by an external magnet composed of two cylindrical NdFeB magnets (45 mm diameter, 30 mm height; N45, Supermagnete), separated by 10 mm. The external magnet is moved in parallel over the MCMs at a 40 mm distance.

Magnetic field gradients are responsible for exerted forces (dB_z/dz) and range from 0.7 to 1 T/m, at a field of 20–30 mT (Fig. 7D), which can be generated by reported electromagnet and permanent magnet based manipulation systems.^{13,54–56} Axial force (f_z), attractive force (f_y), and lateral force (f_x) on the MCMs are shown for offsets (Δ) between the centers of mass of the MCMs and magnet. Measured forces are similar in magnitude, indicating a similar magnetic moment of MCMs. Maximum axial force is 0.09 N. We observe nonzero f_x , which is attributed to misalignment of the axial directions of the permanent magnet and MCM. In addition, we observe a nonsymmetric force profile for f_y and f_z around $\Delta = 0$, which is due to the 10 mm gap between the two cylindrical magnets that make up the permanent magnet.

Finally, the collective contribution of multiple ring magnets on local dipole interactions is analyzed in simulation for

up to five consecutive ring magnets. Ring magnets have relative deflections ($1\text{--}40^\circ$), representing various magnitudes of MCM retroflexion (Fig. 8). Ring magnets are represented in the yz -plane. Bending torques due to collective ring magnet fields ($\tau_{x,B}$) and field gradients ($\tau_{x,B\nabla}$) on the tip magnet are shown in red, and their sum shown in blue. These local gradients act to increase deflection, while local fields act to oppose. Deflection increases as long as the influence of the collective gradient is dominant compared to the collective field. For a set of two ring magnets used in our work, separated by $L = 4$ mm, we observe that the torque due to both field and gradient follows $\tau_{x,B\nabla}$. However, increasing the number of magnets shifts the exerted torque toward $\tau_{x,B}$. Decreasing distance between magnets can prevent $\tau_{x,B}$ becoming dominant, as gradients increase faster than fields with decreasing magnet–magnet distance.

Phantom navigation

MCM maneuverability is shown in a phantom representing the human adult abdominal aorta and compared to an MPC cylinder (0.2 volume fraction). The external magnet (Fig. 7C) is manually moved beneath the phantom (Fig. 9A) at a 30–40 mm distance. The phantom trajectory includes bifurcations with angles up to 135° . The MCM (Fig. 9B) takes on J- and S-shaped forms where the MPC rod is unable to (Supplementary Video S1).

In addition, to show application of the backbone, the MCM is steered from the left common iliac to the superior mesenteric artery where a contrast dye simulant (water with red dye) is released (Fig. 9C; Supplementary Video S1). The simulant is injected with a syringe through the free-hanging backbone from outside the phantom. Then, with the peristaltic pump turned on (flow of 2.7 L/min) the MCM is navigated through the phantom (total path length >50 cm) within 1 min (Fig. 9D). In addition, the backbone may be used as a guiding sheath for, for example, guidewires to reach distal vessel bifurcations (Fig. 9E; Supplementary Video S2). In the future, actuation can be improved by teleoperation of robotically-moved external magnets.⁵⁵ In addition, imaging may be performed with, for example, C-arm fluoroscopy.¹¹

During actuation, we initially experienced significant friction between the MCM and phantom. The friction coefficient between silicone surfaces has been reported to be on the order of 1, while that between catheters and porcine vasculature to be between 0.02 and 0.04.^{57,58} To reduce the friction between the MCM and phantom, we lubricated the phantom with silicone oil. We did not experience hydrodynamic drag forces during navigation, but note that the viscosity of blood in the abdominal aorta may be five times higher than water.⁵⁹ In addition, at a flow of 2.7 L/min the pump revolutions per minute is higher compared to the beats per minute of a heart at rest. Furthermore, the phantom does not mimic material properties of human blood vessels. In reality, movement through vessels may deform them, and possible damaging effects on vessel walls remain to be investigated.

Demonstrations are performed in a 2D phantom. One of the factors that need to be considered for 3D navigation is MCM weight. The presented nine-segment MCM design has a mass of 2.25 g and weight of 0.022 N, which can be lifted

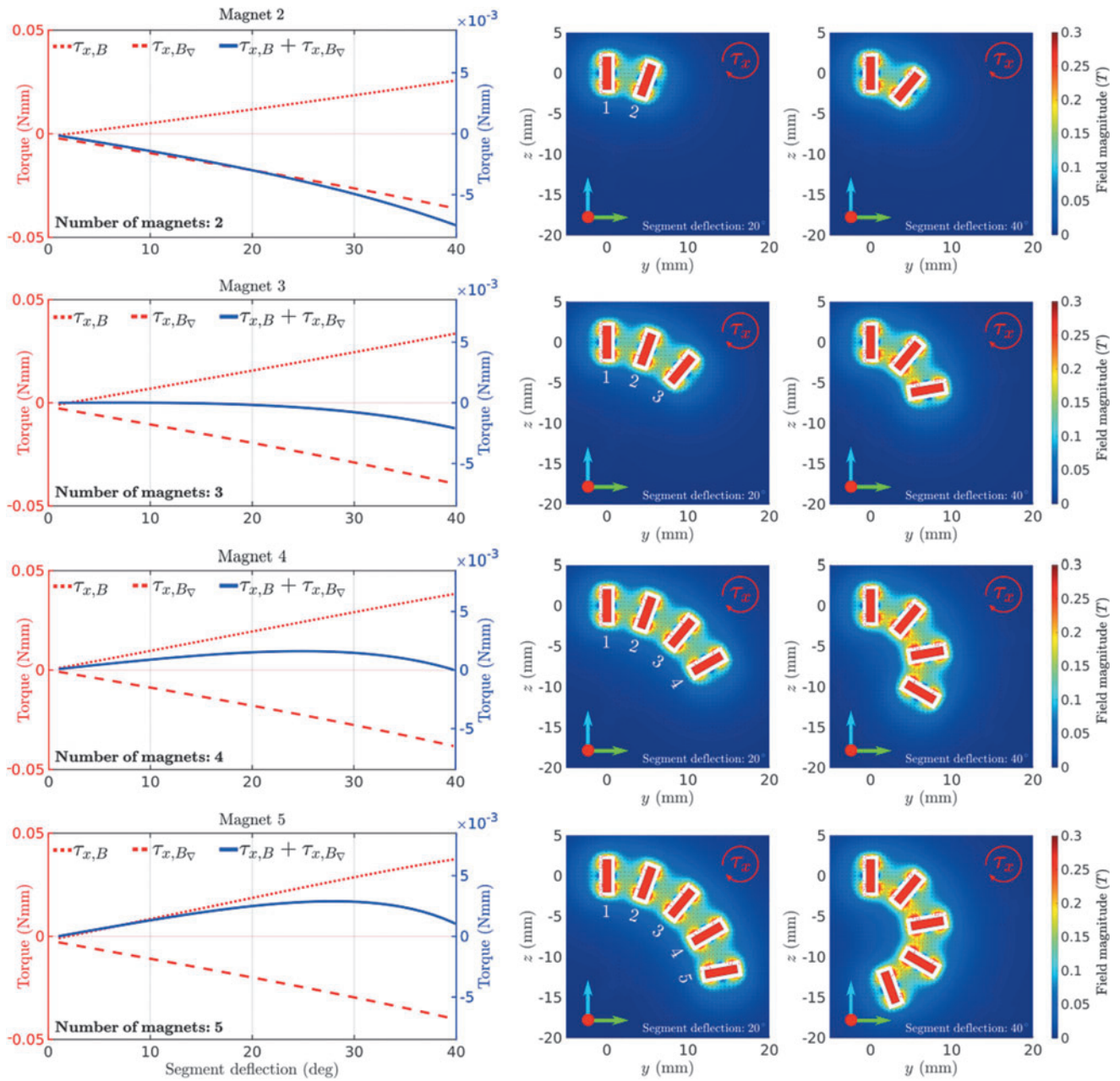


FIG. 8. Simulation analysis of torques exerted on the tip magnet by collective fields ($\tau_{x,B}$) and field gradients ($\tau_{x,B\nabla}$) of preceding magnets. Shown for sets of 2–5 magnets at relative deflections of 1–40°. *Left column* shows bending torques. *Middle column* shows positions of ring magnets with relative deflections of 20°. *Right column* shows positions of ring magnets with relative deflections of 40°. Values are specific to MCM design parameters given in Table 1. Magnetic fields from MPC helices are not included.

using the external magnetic field gradients used in this work. In addition, insertion into vasculature requires an introducer sheath, which will be a source of friction but could be combined with manual or robotic insertion. Finally, we chose to perform MCM demonstrations in a vascular phantom as it allowed workspace-specific MCM design due to the confinement, nonlinear paths, and sharp turns. We note that this decision is theoretically and design motivated, rather than for a specific application. Therefore, the design principles presented herein may be translated to other medical and non-medical environments.

Conclusions

We propose a new design for MCMs that combines permanent magnets and MPC and enables increasing diameter without compromising on flexibility and magnetic moment. The condensed hard magnetic particles inside the MCM enables utilizing magnetic force for actuation. Compared to MPC cylinders, the proposed design uses MPC helices and increases magnetic volume fraction, adds intermittent permanent magnets, and utilizes local dipole interactions between magnets to compensate for additional MPC stiffness.

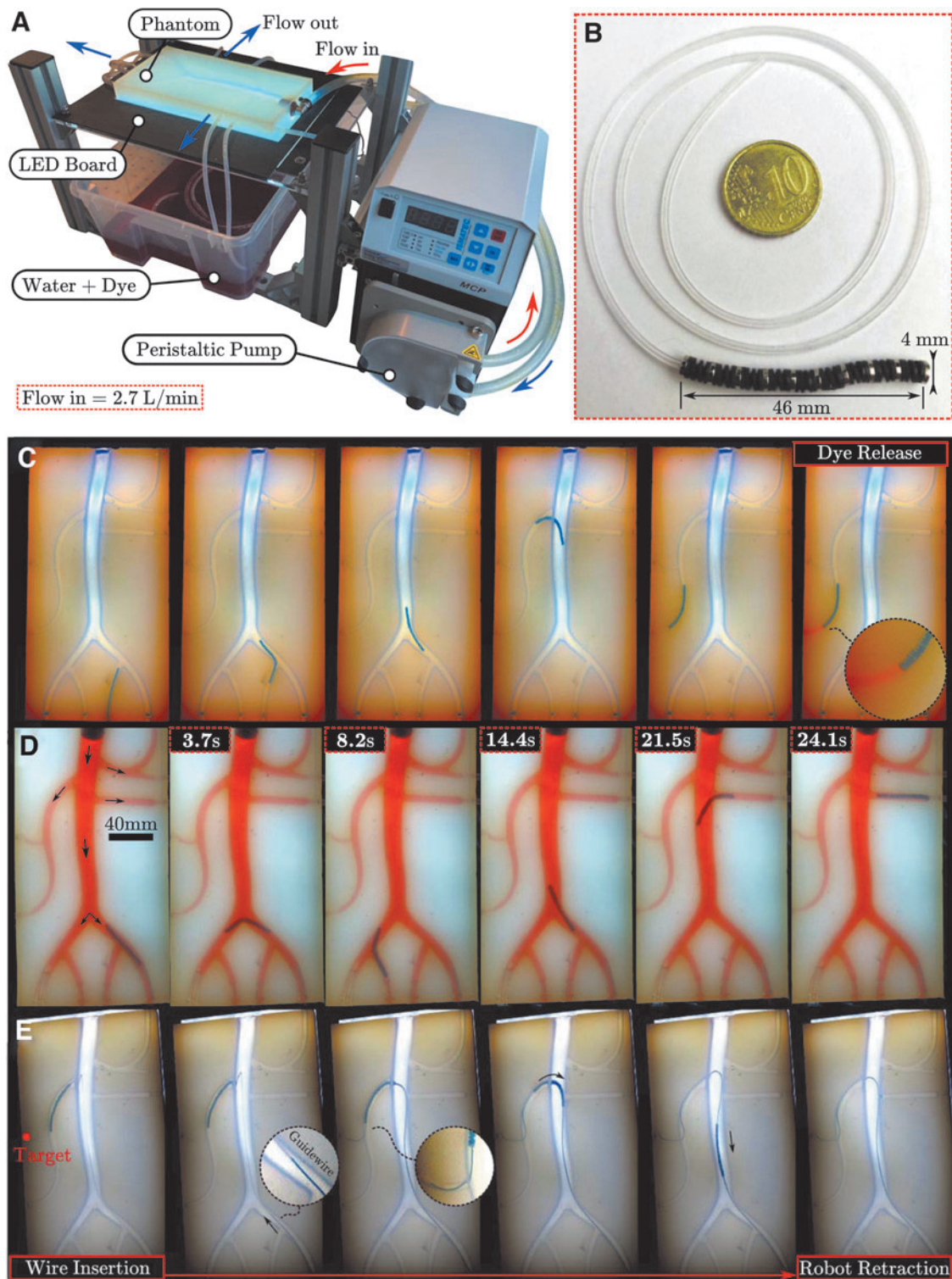


FIG. 9. Navigation experiments. (A) A 2D silicone phantom rests on top of an LED board and is connected to a peristaltic pump. (B) Close up of the assembled MCM with 9 segments: 10 ring magnets and 9 MPC helices. (C) MCM maneuvering using a handheld permanent magnet (Fig. 7C) at a distance of 30–40 mm. A contrast dye simulant (water with dye) is injected through the silicone tube backbone and released at the MCM tip (Supplementary Video S1). (D) MCM maneuvering with the peristaltic pump turned on (2.7 L/min). Direction of flow and the MCM at different time instants are shown. (E) The silicone tube backbone is replaced by a polytetrafluoroethylene backbone for passing of a guidewire. The MCM is retracted after delivery (Supplementary Video S2).

Local dipole interactions between magnets can oppose or promote deflection, depending on dominance of local fields or gradients in exerting bending torques, respectively.

Cosserat rod models can incorporate local dipole interaction effects on segment deflection. The versatility of the model allows changing segment dimensions, magnetic properties, and backbone, depending on intended application. A limitation of the model is that physical bending constraints of segments are not considered. Furthermore, bending torques from collective local fields can increase faster than the local gradients and may become dominant in opposing deflection. Consequently, simulated local dipole interactions within single segments cannot be generalized to multiple connected segments.

In experiments we achieved a 31% increased tip deflection in single segments with local dipole interactions compared to those without. Magnetic forces on the order of 0.09 N at external field gradients of 0.7 T/min were able to navigate the MCM through a silicone phantom (length >50 cm) within 1 min. Although comparisons with MPC cylinders were made regarding maneuverability, the MCM fabrication process is more involved and relatively difficult to apply to submillimeter scales.

In the future, application-specific optimization of the proposed design for both tethered and untethered applications can be studied. While the dipole interaction effect for a particular configuration has been presented, addressing this for other scenarios warrants further investigation. Finally, combining the MCM with backbones made of smart materials, such as thermoset shape memory polymers, may be investigated further.

Author Disclosure Statement

No competing financial interests exist.

Funding Information

This research has received funding from the European Research Council (ERC) under the European Union's Horizon 2020 Research and Innovation programme (Grant Agreement #866494—project MAESTRO).

Supplementary Material

Supplementary Video S1
Supplementary Video S2

References

- Burgner-Kahrs J, Rucker DC, Choset H. Continuum robots for medical applications: A survey. *IEEE Trans Robot* 2015;31(6):1261–1280.
- Dupont P, Simaan N, Choset H, et al. Continuum robots for medical interventions. *Proc IEEE* 2022;110(7):847–870.
- Veiga T. da, Chandler JH, Lloyd P, et al. Challenges of continuum robots in clinical context: A review. *Prog Biomed Eng* 2020;2(3):032003.
- Bruns TL, Ramirez AA, Emerson MA, et al. A modular, multi-arm concentric tube robot system with application to transnasal surgery for orbital tumors. *Int J Rob Res* 2021; 40(2–3):521–533.
- Ataollahi A, Karim R, Fallah AS, et al. Three-degree-of-freedom MR-compatible multisegment cardiac catheter steering mechanism. *IEEE Trans Biomed Eng* 2013;63(11): 2425–2435.
- Ali A, Sakes A, Arkenbout EA, et al. Catheter steering in interventional cardiology: Mechanical analysis and novel solution. *Proc Inst Mech Eng H* 2019;233(12):1207–1218.
- Campisano F, Cal S, Ramirez AA, et al. Closed-loop control of soft continuum manipulators under tip follower actuation. *Int J Rob Res* 2021;40(6–7):923–938.
- Garbin N, Wang L, Chandler JH, et al. A disposable continuum endoscope using piston-driven parallel bellow actuator. In: *Proceedings of the International Symposium on Medical Robotics*. IEEE: Atlanta, GA, USA; 2018; pp. 1–6.
- Kim Y, Parada GA, Liu S, et al. Ferromagnetic soft continuum robots. *Sci Robot* 2019;4(33):eaax7329.
- Pancaldi L, Dirix P, Fanelli A, et al. Flow driven robotic navigation of microengineered endovascular probes. *Nat Commun* 2020;11(1):1–14.
- Hwang J, Jeon S, Kim B, et al. An electromagnetically controllable microrobotic interventional system for targeted, real-time cardiovascular intervention. *Adv Healthc Mater* 2022;11(11):2102529.
- Phelan III MF, Tiryaki ME, Lazovic J, et al. Heat-mitigated design and Lorentz force-based steering of an MRI-driven microcatheter toward minimally invasive surgery. *Adv Sci* 2022;9(10):2105352.
- Azizi A, Tremblay CC, Gagn K, et al. Using the fringe field of a clinical MRI scanner enables robotic navigation of tethered instruments in deeper vascular regions. *Sci Robot* 2019;4(36):eaax7342.
- Carpi F, Pappone C. Stereotaxis Niobe magnetic navigation system for endocardial catheter ablation and gastrointestinal capsule endoscopy. *Expert Rev Med Devices* 2009; 6(5):487–498.
- Chautems C, Tonazzini A, Boehler Q, et al. Magnetic continuum device with variable stiffness for minimally invasive surgery. *Adv Intell Syst* 2020;2(6):1900086.
- Charreyron SL, Boehler Q, Danun AN, et al. A magnetically navigated microcannula for subretinal injections. *IEEE Trans Biomed Eng* 2020;68(1):119–129.
- Heunis CM, Behrendt K, Hekman E, et al. Design and evaluation of a magnetic rotablation catheter for arterial stenosis. *IEEE ASME Trans Mechatron* 2021;27(3):1761–1772.
- Sikorski J, Heunis CM, Obeid R, et al. A flexible catheter system for ultrasound-guided magnetic projectile delivery. *IEEE Trans Robot* 2021;38(3):1959–1972.
- Mattmann M, De Marco C, Briatico F, et al. Thermoset shape memory polymer variable stiffness 4D robotic catheters. *Adv Sci* 2022;9(1):2103277.
- Li Y, Guo C, Xin W, et al. Design and preliminary evaluation of an electromagnetically actuated soft-tethered colonoscope. *IEEE Trans Med Robot Bionics* 2021;3(2): 402–413.
- Martin JW, Scaglioni B, Norton JC, et al. Enabling the future of colonoscopy with intelligent and autonomous magnetic manipulation. *Nat Mach Intell* 2020;2(10):595–606.
- Barducci L, Pittiglio G, Norton JC, et al. Adaptive dynamic control for magnetically actuated medical robots. *IEEE Robot Autom Lett* 2019;4(4):3633–3640.
- Hwang J, Kim J-y, Choi H. A review of magnetic actuation systems and magnetically actuated guidewire-and catheter-based microrobots for vascular interventions. *Intell Serv Robot* 2020;13(1):1–14.

24. Jeon S, Hoshier AK, Kim K, et al. A magnetically controlled soft microrobot steering a guidewire in a three-dimensional phantom vascular network. *Soft Robot* 2019; 6(1):54–68.
25. Heunis CM, Sikorski J, Misra S. Flexible instruments for endovascular interventions: Improved magnetic steering, actuation, and image-guided surgical instruments. *IEEE Robot Autom Mag* 2018;25(3):71–82.
26. Le VN, Nguyen NH, Alameh K, et al. Accurate modeling and positioning of a magnetically controlled catheter tip. *Med Phys* 2016;43(2):650–663.
27. Yang Z, Yang L, Zhang M, et al. Magnetic control of a steerable guidewire under ultrasound guidance using mobile electromagnets. *IEEE Robot Autom Lett* 2021;6(2): 1280–1287.
28. Zhang T, Yang L, Yang X, et al. Millimeter-scale soft continuum robots for large-angle and high-precision manipulation by hybrid actuation. *Adv Intell Syst* 2021;3(2): 2000189.
29. Kim Y, Yuk H, Zhao R, et al. Printing ferromagnetic domains for untethered fast-transforming soft materials. *Nature* 2018;558(7709):274–279.
30. Wu S, Hu W, Ze Q, et al. Multifunctional magnetic soft composites: A review. *Multifunct Mater* 2020;3(4):042003.
31. Kim Y, Zhao X. Magnetic soft materials and robots. *Chem Rev* 2022;122(5):5317–5364.
32. Lum GZ, Ye Z, Dong X, et al. Shape-programmable magnetic soft matter. *Proc Natl Acad Sci* 2016;113(41): E6007–E6015.
33. Lloyd P, Hoshier AK, da Veiga T, et al. A learnt approach for the design of magnetically actuated shape forming soft tentacle robots. *IEEE Robot Autom Lett* 2020;5(3):3937–3944.
34. Wang L, Zheng D, Harker P, et al. Evolutionary design of magnetic soft continuum robots. *Proc Natl Acad Sci* 2021; 118(21):e2021922118.
35. Sikorski J, Heunis CM, Franco F, et al. The ARMM system: An optimized mobile electromagnetic coil for non-linear actuation of flexible surgical instruments. *IEEE Trans Magn* 2019;55(9):1–9.
36. Gosselin FP, Lalande V, Martel S. Characterization of the deflections of a catheter steered using a magnetic resonance imaging system. *Med Phys* 2011;38(9):4994–5002.
37. Till J, Aloï V, Rucker C. Real-time dynamics of soft and continuum robots based on Cosserat rod models. *Int J Rob Res* 2019;38(6):723–746.
38. Edelmann J, Petruska AJ, Nelson BJ. Magnetic control of continuum devices. *Int J Rob Res* 2017;36(1):68–85.
39. Richter M, Venkiteswaran VK, Misra S. Multi-point orientation control of discretely-magnetized continuum manipulators. *IEEE Robot Autom Lett* 2021;6(2):3607–3614.
40. Gent AN. On the relation between indentation hardness and Young's modulus. *Rubber Chem Technol* 1958;31(4):896–906.
41. Mooney M. The viscosity of a concentrated suspension of spherical particles. *J Colloid Sci* 1951;6(2):162–170.
42. Deswal A, Tamang BK, Bala A. Study of aortic-common iliac bifurcation and its clinical significance. *J Clin Diagn Res* 2014;8(7):AC06.
43. Dyches RP, Eaton KJ, Smith HF. The roles of celiac trunk angle and vertebral origin in median arcuate ligament syndrome. *Diagnostics* 2020;10(2):76.
44. Ekingen A, Hatipoglu ES, Hamidi C. Distance measurements and origin levels of the coeliac trunk, superior mesenteric artery, and inferior mesenteric artery by multiple-detector computed tomography angiography. *Anat Sci Int* 2021;96(1): 132–141.
45. Desai AB, Shah DS, Bhatt CJ, et al. Measurement of the distance and angle between the aorta and superior mesenteric artery on CT scan: Values in Indian population in different BMI categories. *Ind J Surg* 2015;77(2):614–617.
46. Reymond P, Merenda F, Perren F, et al. Validation of a one-dimensional model of the systemic arterial tree. *Am J Physiol Heart Circ Physiol* 2009;297(1):H208–H222.
47. Suh G-Y, Choi G, Herfkens RJ, et al. Three-dimensional modeling analysis of visceral arteries and kidneys during respiration. *Ann Vasc Surg* 2016;34:250–260.
48. Richardson Jr R, Miller J, Reichert WM. Polyimides as biomaterials: Preliminary biocompatibility testing. *Biomaterials* 1993;14(8):627–635.
49. Venzac B, Deng S, Mahmoud Z, et al. PDMS curing inhibition on 3D-printed molds: Why? Also, how to avoid it? *J Analyt Chem* 2021;93(19):7180–7187.
50. Sikorski J, Dawson I, Denasi A, et al. Introducing BigMag-A novel system for 3D magnetic actuation of flexible surgical manipulators. *Proc Int Conf Robot Autom. IEEE: Marina Bay Sands, Singapore; 2017; pp. 3594–3599.*
51. Sikorski J, Denasi A, Bucchi G, et al. Vision-based 3-D control of magnetically actuated catheter using BigMag—An array of mobile electromagnetic coils. *IEEE ASME Trans Mechatron* 2019;24(2):505–516.
52. Saggiomo V, Velders AH. Simple 3D printed scaffold-removal method for the fabrication of intricate microfluidic devices. *Adv Sci* 2015;2(9):1500125.
53. Taylor CA, Cheng CP, Espinosa LA, et al. In vivo quantification of blood flow and wall shear stress in the human abdominal aorta during lower limb exercise. *Ann Biomed Eng* 2002;30(3):402–408.
54. Erni S, Schrlie S, Fakhraee A, et al. Comparison, optimization, and limitations of magnetic manipulation systems. *J Microbio Robot* 2013;8(3–4):107–120.
55. Kim Y, Genevriere E, Harker P, et al. Telerobotic neurovascular interventions with magnetic manipulation. *Sci Robot* 2022;7(65):eabg9907.
56. Gang ES, Nguyen BL, Shachar Y, et al. Dynamically shaped magnetic fields: Initial animal validation of a new remote electrophysiology catheter guidance and control system. *Circ Arrhythm Electrophysiol* 2011;4(5):770–777.
57. Penskiy I, Gerratt A, Bergbreiter S. Friction, adhesion and wear properties of PDMS films on silicon sidewalls. *J Micromech Microeng* 2011;21(10):105013.
58. Lin C, Kaper HJ, Li W, et al. Role of endothelial glycocalyx in sliding friction at the catheter-blood vessel interface. *Sci Rep* 2020;10(1):1–10.
59. Connes P, Alexy T, Detterich J, et al. The role of blood rheology in sickle cell disease. *Blood Rev* 2016;30(2):111–118.

Address correspondence to:

Michiel Richter
Surgical Robotics Laboratory
Department of Biomechanical Engineering
University of Twente
7500 AE Enschede
The Netherlands

E-mail: m.richter@utwente.nl